Electronic Supplementary Material (ESI) for RSC Advances.

ESI-1: The lattice parameter *a* and *c*; interplanar spacing (d_{100}, d_{002}, and d_{101}); unit cell volume (V); *u* (length of the bond parallel to the *c* axis, in units of *c*); bond distance (*R*) and bond angles ($^{O_a\text{-}Zn\text{-}O_b \; and \; O_b\text{-}Zn\text{-}O_b}$) calculated from XRD data:

Parameters	**Sample**			
	Co0	**Co0 (5×10^{12})**	**Co2**	**Co2 (5×10^{12})**
a (Å)	3.2416	3.2575	3.2467	3.2463
c (Å)	5.1959	5.2179	5.2008	5.2002
c/a	1.6021	1.6018	1.6019	1.6019
d_{100} (Å)	2.8074	2.8211	2.8096	2.8193
d_{002} (Å)	2.5980	2.6090	2.5998	2.6069
d_{101} (Å)	2.4705	2.4814	2.4727	2.4802
V (Å^3)	47.2834	47.9503	47.4777	47.4609
u	0.3799	0.3799	0.3799	0.3799
$R_{Zn\text{-}O_a}$ *(Å)*	1.9752	1.9824	1.9758	1.9756
$R_{Zn\text{-}O_b}$*(Å)*	1.9753	1.9824	1.9758	1.9756
$O_a\text{-}Zn\text{-}O_b$ (°)	108.4373	108.4269	108.4290	108.4293
$O_b\text{-}Zn\text{-}O_b$ (°)	110.4850	110.4951	110.4931	110.4928

ESI-2: The liner fit $(d\beta Cos\theta/\lambda)^2$ vs. $(d^2\beta Cos\theta/\lambda^2)$ plot of the samples to estimate crystallite size and strain.

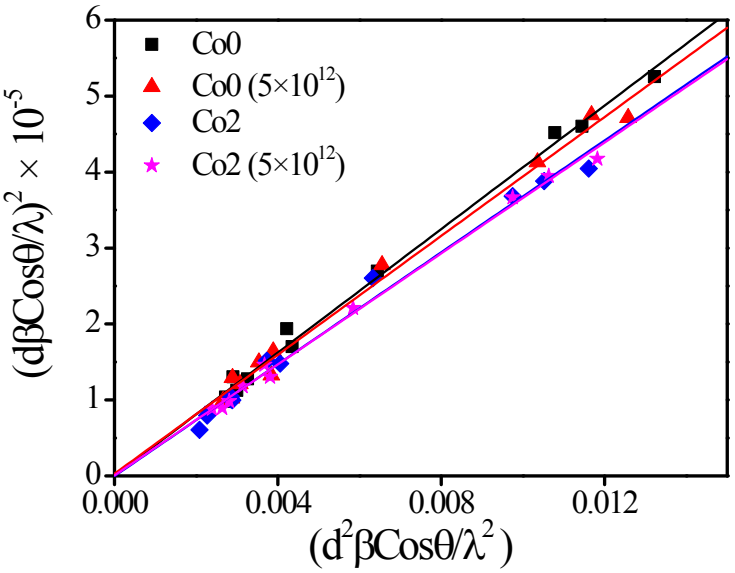

ESI-3: Intensity ratios of some of the Raman modes:

Sample	$\left(\frac{E_{2H}-E_{2L}}{E_{2H}}\right)$		$\left(\frac{A_1(LO)}{E_{2H}}\right)$		$\frac{(E_{2H}-E_{2L})_I}{(E_{2H}-E_{2L})_P}$	$\frac{(E_{2H})_I}{(E_{2H})_P}$	$\frac{(A_{1\,(LO)})_I}{(A_{1\,(LO)})_P}$
	Pristine	**Irradiated**	**Pristine**	**Irradiated**			
ZnO	0.130	0.277	0.175	2.642	0.226	0.106	1.599
$Zn_{0.98}Co_{0.02}O$	0.203	0.226	0.268	0.727	0.932	0.836	2.270

ESI-4:. Different Vibrational Modes of FTIR study:

ZnO		**$Zn_{0.98}Co_{0.02}O$**		**Modes (cm^{-1})**
Pristine Co0	**Irradiated Co0 (5×10^{12})**	**Pristine Co2**	**Irradiated Co2 (5×10^{12})**	
475	475	467	480	Zn-O bond (teradehral)
670	665	672	668	Zn-O bond (octahedral)
----	805	----	802	Co-O bond
874	864	873	865	Citrate precursor
----	1050	----	1050	Co-O bond
----	1260	----	1260	Co-O bond
1385	1380	1385	1385	Asymmetric stretching of C=C in citrate
1632	1625	1595	1632	Stretching mode of –OH
2345	2345	2345	2342	CO_2 molecules in air
2852	2856	2832	2832	C-H bond bending
2927	2922	2927	2924	C-H bond stretching
----	2964	----	2964	Co-O bond
3458	3480	3461	3472	O-H bond

ESI-5:.

Investigations on structural and optical properties of ZnO and ZnO:Co nanoparticles under dense electronic excitations

Shiv Kumar,[a] Kandasami Asokan,[b] Ranjan Kumar Singh,[a] Sandip Chatterjee,[c] Dinakar Kanjilal[b] and Anup Kumar Ghosh[*a]

[a] *Materials Research Lab. Department of Physics, Banaras Hindu University, Varanasi-221 005, India.*
[b] *Inter University Accelerator Centre, Aruna Asaf Ali Marg, New Delhi 110 067, India*
[c] *Department of Applied Physics, Indian Institute of Technology, Banaras Hindu University, Varanasi-221 005, India*

Abstract

In the present study, the structural, morphological, and optical properties of Co-doped ZnO nanoparticles (NPs) prepared by sol-gel method before and after dense electronic excitations caused by swift heavy ion irradiation have been reported. The pristine and ZnO:Co NPs were irradiated by using 200 MeV Ag^{15+} ion beam at fluence of 5×10^{12} ions/cm^2. Structural characterization has been performed by using X-ray diffraction (XRD) with Rietveld refinement. It shows that the samples are of single phase; grain size and tensile strain has been increased in the ion-irradiated samples. Room temperature Raman spectroscopy measurements show that microscopic structural disorders reduce the translational symmetry giving rise to local distortions in the lattice. Atomic force microscopic (AFM) studies show prominent grain boundaries and suggest that roughness of the irradiated surfaces increases strongly compared to their pristine counterparts. Optical absorption and photoluminescence (PL) studies also reflect the dopant incorporation and swift heavy ion (SHI) irradiation effect on the nanoparticles. UV-Vis absorption measurement has been utilized to estimate the optical bandgap of pristine and irradiated ZnO and Co-doped ZnO nanoparticles. Enhancement in the PL intensity has been observed in the irradiated samples with respect to pristine counterparts which can be explained on the basis of the increase of different defect states and Zn–O bonds on the surfaces of the irradiated nanoparticles arising from surface modification. Grain boundaries have played an important role in the optical properties (absorption and PL).

PACS No: 61.05.Cp, 73.63.Bd, 74.25.nd, 78.30.-J, 78.40.-q

Keywords: Sol-gel; Ion irradiation; ZnO nanoparticles; Structural properties; Raman study; Optical properties.

*Corresponding author: Anup K. Ghosh (akghosh@bhu.ac.in; anupkg66@gmail.com).

Introduction

Diluted magnetic semiconductors (DMSs)[1] are compounds in which a very small fraction of non-magnetic ions is replaced by magnetic ions (typically transition metal (TM) ions such as Fe, Mn, Co etc. and rare earth metal ions). In DMSs magnetic ions are randomly distributed and show typical semiconductor behaviour as well as pronounced magnetic properties. The most important feature of DMSs are the co-existence and interaction of two different electronic subsystems namely delocalized conduction band (*s*-type) and valence band (*p*-type) electrons and localized (*d*- or *f*-type) electrons of magnetic ions[1]. The applicability of DMSs has been limited due to the very low value of Curie temperature (T_c~170 K). The realization of DMSs having Curie temperature above the room temperature will potentially lead to a new generation of spintronics devices with revolutionary electrical and optical properties.

Theoretical calculations, based on Zener model of magnetism with holes mediated exchange interaction, predicted the possibility of room temperature ferromagnetism in TM doped ZnO (II–VI) and GaN (III–V) or more generally in wide band gap semiconductors[2]. In the past decades, ZnO-based DMSs[1] are considered to be one of the most promising materials for ultraviolet LEDs[3], laser diodes, spintronics and many other spin-based devices[4,5] because of its large band gap (3.36 eV) and high exciton binding energy (60 meV). ZnO is an optically transparent II–VI semiconductor and well-known piezoelectric and electro-optic material having hexagonal wurtzite structure with C^4_{6v} ($P6_3mc$) space group. Studies of different physical properties (such as structural, optical, magnetic properties etc.) based on different TM (such as Cr, Mn, Fe, Co etc.) doped ZnO have been explored by various researchers.[6-11] Doping of semiconductor with TM elements offers a practicable means of tuning the optical properties as well as the ferromagnetism. Sharma et al.[9] demonstrated that 1% Fe doped ZnO samples show diamagnetic character, while weak ferromagnetic nature is observed for 2, 3 and 4% Fe doped ZnO. Kim *et al.*[10] have shown room temperature ferromagnetism (RTFM) in $Zn_{1-x}Co_xO$ thin film and suggested that this RTFM was resulted from the impurity in form of Co clusters. The

intrinsic ferromagnetism has been observed by Zhang *et al.*[11] in Co-doped ZnO nanoparticles. Though, ferromagnetism in DMSs is a burning topic to be resolved, structural and optical properties are also very important properties for device applications.

On the other hand, ion beam irradiation is one of the important techniques that are being used effectively to create a wide variety of defect states in the materials which induce change in their structural, optical, and many other properties[12-14]. These changes are strongly dependent on the mass of the incident ions, irradiation energy loss mechanism of the system and fluence. In this technique ions with energy in the range of keV to a few MeV collide with the target. When a swift heavy ion (SHI) penetrates a solid, it becomes slow via two processes either direct transfer of energy to the target atoms through elastic collision or electronic excitation and ionization of target atoms by the inelastic collision[15,16]. The latter one is more dominant in the case of SHI. The energy transfer is mainly due to electronic energy loss if and when the thickness of the targeted medium is much smaller than the range of the projectile ion. This dense electronic excitations transfer electronic energy and leads to the creation of defects[7] and generation of heat in the material[14,17]. Defects induced by SHI irradiation in DMSs definitely will show some interesting physical properties be studied.

In the present work, we have focused to investigate the effect of 200 MeV Ag^{15+} ion irradiation on the structural and optical properties (such as optical band gap and photoluminescence) of the undoped and Co-doped ZnO samples. For studies of structural, morphological and optical properties XRD, FTIR, Raman spectroscopy, AFM, UV-Vis and PL spectroscopy have been employed.

Experimental details

Synthesis of nanoparticles

All the reactants and solvents were analytical grade. Samples of $Zn_{1-x}Co_xO$ (x=0 and 0.02) (named as Co0 and Co2 respectively) were synthesized by using the sol-gel method. Appropriate proportions of metal nitrates $Zn(NO_3)_2 \cdot 6H_2O$ (99.9% purity) and $Co(NO_3)_2.4H_2O$ (99.9% purity) powders were thoroughly mixed and dissolved in double distilled water. The prepared solution of metal nitrates was poured in aqueous solution of citric acid [$C_6H_8O_7$] (99.5% purity) while stirring to obtain a homogeneous precursor solution. Citric acid was served as fuel for the reaction. The precursor solution was dried at 80 °C for 3 hrs to obtain xerogel and

the swelled xerogel was kept at 130 °C for 12 hrs to complete drying. After grinding, the xerogel powders were sintered at 600 °C for 10 hrs under air atmosphere to get $Zn_{1-x}Co_xO$ NPs.

Irradiation experiment

Ion beam irradiation experiments were performed by using 15UD Tandem Pelletron Accelerator at Inter University Accelerator Centre, New Delhi (India) to study the effect of irradiation on structural and optical properties of the samples. The samples were irradiated in the Materials Science beam line chamber under a high vacuum (pressure of ~10^{-6} mbar) using 200 MeV Ag^{15+} ion beams with a beam current of ~1 pnA (i.e. particle-nanoampere). The ion-beam fluence was measured by integrating the ion charge on the sample ladder, which was insulated from the chamber. The samples were irradiated with the fluence of 5×10^{12} ions/cm^2 at room temperature. A beam of uniform irradiation covers the entire sample surface. Irradiated $Zn_{1-x}Co_xO$ samples were named as Co0 (5×10^{12}) and Co2 (5×10^{12}) for x=0 and x=0.02 corresponding to the pristine samples Co0 and Co2 respectively.

Characterizations

The study of phase purity of pristine and irradiated $Zn_{1-x}Co_xO$ (x=0, 0.02) samples was performed by X-ray diffractometer (Model: Miniflex-II, Rigaku, Japan) with Cu Kα radiation (λ = 1.5406 Å) operating at 40 kV and 30 mA. Raman spectra were taken in the range of 200–1250 cm^{-1} with a Renishaw micro-Raman spectroscope using 514.5 nm Ar^+ laser as excitation source. Pellets of the samples have been taken for the Raman spectroscopy measurement. Surface morphology was studied using an atomic force microscope (AFM, Digital Instruments Nanoscope IIIa) in the tapping mode. Fourier transmission infrared (FT-IR) spectra of the samples (as pellets in KBr) were recorded using FT-IR Spectrometer (Spectrum One, Perkin Elmer Instrument, USA) in the range of 4000-400 cm^{-1}. The optical absorption spectra were measured in the range of 300-800 nm by using UV-Vis spectrometer (Perkin Elmer Instrument, Lamda-25, USA). The PL spectra were taken by a Fluorescence Spectrometer (LS-45, Perkin Elmer, USA).

Results and discussion

X-ray diffraction studies

For the structural informations and phase identification, pristine and 200 MeV Ag^{15+} ion irradiated NPs of undoped and Co-doped ZnO have been studied by X-ray diffraction (XRD) pattern. The Rietveld refinement of XRD patterns of pristine and irradiated undoped-ZnO samples are shown in Fig. 1(a) while those of Co-doped ZnO samples are shown in Fig. 1(b). The Rietveld refinement of XRD data shows that Co-doping does not lead to the appearance or disappearance of any of the wurtzite peaks which confirms that all the samples remain in hexagonal wurtzite structure belonging to the C^4_{6v} space group ($P6_3mc$) (file No. 186). All XRD peaks have been indexed using the standard JCPDS file (No: 36-1451 shown for ready reference) for ZnO. The open circles correspond to the experimental data points and the solid line through the circles is the results of the Rietveld analysis. The vertical ticks below the curve of Fig. 1(a) and (b) indicate the expected peak positions for the wurtzite phase while the line below the vertical ticks shows the difference pattern of experimental data and calculated profile. All strong peaks have small shift towards lower angle for the Co-doped pristine ZnO compared to undoped pristine ZnO. It may be due to the incorporation of dopant ions (Co ions) into the lattice of the host material[18,19] and strain developed in the lattice. Broadening of the XRD peaks is decreased with Co-doping which may be due to increase of grain size.[20] All the strong peaks in the XRD pattern for the irradiated samples have been shifted towards lower angle with respect to its corresponding pristine samples. The values of inter-planner spacing (*d*-value) calculated from XRD data for (100), (002) and (101) planes show that *d*-value increases due to SHI irradiation. This observation can be explained on the basis of distortion of the tetrahedron. The distortion of the tetrahedron, arising from the variation of bond lengths and bond angles between atoms, develops the lattice strain.[20,21] According to Bragg's law, the Bragg angle should either decrease or increase if the spacing of the crystallographic planes changes. Hence, the tensile stress increases the *d*-spacing which causes a shifting of peak towards lower 2θ values whereas compression stress decreases the *d*-spacing which results the shifting of peaks towards higher 2θ values in the XRD pattern. Lattice parameters '*a*' and '*c*' and inter-planner spacing of different planes have been estimated with the help of Rietveld refinement analysis. Values of different bond angles and bond lengths have been calculated following Morkoç and Özgür[22,23] [see electronic supporting informations (ESI)-1].

The crystallite size, D, of the samples are estimated from XRD line width of (101) peak by using Scherrer's equation:[24,25]

$$D = \frac{0.9\lambda}{\beta_{hkl}\, Cos\theta} \qquad (1)$$

where, λ is the wavelength of radiation used (λ = 1.5406 Å), θ the Bragg angle and β_{hkl} is the full width (instrumental corrected breadth of the reflection located at 2θ) at half maxima (FWHM) given by[21]:

$$\beta_{hkl} = \left[\beta^{2}_{hkl\, measured} - \beta^{2}_{instrumental}\right]^{1/2}$$

It should be pointed out that XRD peaks are symmetric in shape and can be well fitted by the pseudo Voigt and Gaussian functions which have shown in the inset of Fig. 1(a) and 1(b) for (101) plane of the corresponding samples.

A better estimation of the average crystallite size and strain parameters have been achieved from 'size-strain plot' (SSP)[26] by using the following equation:

$$\left(\frac{d_{hkl}\beta_{hkl}Cos\theta}{\lambda}\right)^2 = \frac{k\lambda}{D}\left(\frac{d^2_{hkl}\beta_{hkl}Cos\theta}{\lambda^2}\right) + \left(\frac{\varepsilon}{2}\right)^2 \qquad (2)$$

where, d_{hkl} is the interplaner spacing and ε is the average strain produced in the lattice. β_{hkl}, λ and D are described as earlier, k is the Scherrer constant (= 0.9).

The average crystallite size (D) and average strain (ε) have been estimated from the slope and the intercept of the linear fit of the $\left(\frac{d_{hkl}\beta_{hkl}Cos\theta}{\lambda}\right)^2$ vs $\left(\frac{d^2_{hkl}\beta_{hkl}Cos\theta}{\lambda^2}\right)$ plot respectively [see (ESI) -2].

Raman spectroscopy

The room temperature Raman spectra of pristine and irradiated ZnO and $Zn_{0.98}Co_{0.02}O$ samples are obtained in the backscattering geometry. According to the group theory, ZnO in the wurtzite structure (having 4 atoms per unit cell) belongs to C^4_{6v} space group with all atoms occupying C_{3v} sites. Wurtzite ZnO have the total number of 12 phonon modes namely, one longitudinal-acoustic (LA), two transverse-acoustic (TA), three longitudinal-optical (LO), and six transverse-optical (TO) branches. The zone-center optical phonons of the wurtzite structure

of ZnO can be classified according to the irreducible representation as[27]: $\Gamma_{opt} = A_1+2B_1+E_1+2E_2$. Both the A_1 and E_1 modes are polar and can be split into transverse optical (TO) and longitudinal optical (LO) phonons with all being the Raman and infrared active. Non-polar E_2 modes are Raman active while the B_1 modes are silent in Raman scattering. The vibration of oxygen sublattice gives rise to high-frequency E_2 mode [viz. E_2 (high) or E_{2H}] which is the strongest mode and characteristic of the wurtzite structure whereas that of heavy Zn sublattice gives rise to the low-frequency E_2 [viz. E_2 (low) or E_{2H}] mode.[28,29] The wurtzite ZnO NPs have six Raman-active phonon modes reported at 101cm^{-1} (E_2 low), 381 cm^{-1} (A_1 TO), 407 cm^{-1} (E_1 TO), 437 cm^{-1} (E_2 high viz. E_{2H}), 574 cm^{-1} (A_1 LO), and 583 cm^{-1} (E_1 LO) respectively.[29,30] Fig. 2 shows the room-temperature Raman spectra of pristine and irradiated ZnO and $Zn_{0.98}Co_{0.02}O$ (inset) samples in the range of 200-1400 cm^{-1}. The positions of phonon vibrational frequencies and their assignments have been summarized in Table-2. Most of the prominent peaks of pristine ZnO are also observed in pristine Co-doped NPs. However, most of the Raman modes become relatively less intense (weak) without appreciable shifting and broadening in frequency for Co-doped NPs (pristine) sample compared to pristine ZnO samples. This is due to the fact that Co-doping did not change the crystal structure (wurtzite) of ZnO lattice. The peak observed at 329 cm^{-1} is related to the single-crystalline nature of ZnO[29,31] and has been assigned as a difference mode between the E_2-high and E_2-low frequencies,[32,33] viz.(E_{2H} − E2L). The fundamental optical modes in the pristine ZnO are E_1(TO) at ~408 cm^{-1} (very weak peak) and A_1(LO) at ~576 cm^{-1} [34] An another peak has been observed at 585 cm^{-1} [E_1(LO) mode]. The intensity of A_1(LO) mode has decreased in Co-doped ZnO as compared to pristine ZnO. The broad shoulder appears at ~658 cm^{-1} for ZnO may be due to the two-phonon process[35]. It has also been noticed that the shoulder centered at ~658 cm^{-1} (second-order mode for ZnO) shifts toward higher frequency (682 cm^{-1}) for Co–doped pristine samples (see Table 3(a)). The other second-order mode at ~1142 cm^{-1} for ZnO has not changed appreciably (~1148 cm^{-1}) for Co-doped ZnO (pristine). It should be noted here that we have assigned the modes as second order, whose frequency is close to the double of any first-order mode. After irradiation (both pure and Co-doped samples) the intensity of the non-polar E_{2H} mode decreases and shift towards higher frequency while the intensity of (E_{2H}-E_{2L}) mode did not change after irradiation. The shifts in higher frequency may due to the tensile strain induced[36,37] in the irradiated samples than the pristine one. This corroborates the result obtained from the XRD measurement. The intensity of peaks around 490,

575 and 705 cm^{-1} has been increased which may be due the fact that ion irradiation induces a microscopic structural disorder and gives rise to local distortions in the lattice. To quantify these variations, the ratios of some of the Raman peak-intensities have been calculated (ESI-3).

Surface morphology

The surface topography of the pristine and irradiated ZnO and Co-doped ZnO have been studied using Atomic Force Microscopy (AFM) in the tapping mode. AFM data analysis gives the quantitative information about the surface morphology. 2-dimensions (2D) and 3- dimensions (3D) AFM micrographs of pristine and irradiated pure ZnO [Fig. 3] and Co-doped ZnO [Fig. 4] samples clearly show that the obtained samples are indeed nano-grained and contain, very developed grain boundaries and free surfaces. It has been recently demonstrated that the physical properties of pure and doped nano-grained ZnO strongly depend on the presence of defects like inter-phase boundaries and grain boundaries[38] and on the presence of doping atoms in the inter-ficial and inter-granular layers[39]. Therefore, it is expected that these developed grain boundaries and free surfaces will also play an important role for the physical properties of our samples. The AFM study also shows the change in surface morphology due to the swift heavy ion beam irradiation. Roughness of the pellets was estimated with Nanoscope 5.31r1. Scans over 2×2 μm^2 were taken for measuring the surface roughness of the pellets. The root-mean-square roughness (R_{RMS}) has been estimated by using the formula[40]:

$$R_{RMS} = \sum_{i=1}^{N}\left[\frac{(h_i - \bar{h})^2}{N}\right]^{1/2} \qquad (3)$$

where h_i and $\bar{h}$ represents the height value at each data point and the profile mean value of the surface respectively; N is the number of data points in the analyzed profile. The standard roughness or the arithmetic average roughness-height, represents the arithmetic mean of the deviations in height from the profile mean value, where the profile mean value is defined as[40]:

$$\bar{h} = \frac{1}{N}\sum_{i=1}^{N} h_i \qquad (4)$$

The root-mean-square roughness (R_{RMS}) estimated for the pellets of Co0 and Co0 (5×10^{12}) are 19 and 30 nm respectively while those for the doped samples viz. Co2 and Co2 (5×10^{12}) are found to be ~16 and ~28 nm respectively. The AFM study shows that the roughness (R_{RMS}) increases

after the irradiation. Similar observation was reported earlier.[41,42] This increase in the surface roughness may be due to the damage and defects created by the Ag ions on the surface of the nanoparticles. [41,42]

FT-IR spectroscopy

FT-IR spectroscopy has been employed to study the functional group present in the compound, inter- or intra-molecular interactions, molecular geometry, the vibrational bands due to Zn–O bond, and the changes due to Co substitution in its structure before and after irradiation at room temperature. The KBr pellet technique has been used to record the spectra. Figure 5 represents the FTIR spectra of pristine and irradiated pure and Co-doped ZnO nanoparticles. The sharp absorption peak at around 475 cm^{-1} and relatively weak absorption peak at ~670 cm^{-1} are assigned to stretching modes of Zn–O in the tetrahedral and octahedral coordination respectively.[43-45] From fig. 5 it is observed that the tetrahedral coordination (in both pristine and irradiated samples) is stronger and dominating as compared with its octahedral counterpart. Due to Co-doping, the peak ~670 cm^{-1} (octahedral coordination) does not change significantly which implies that the Co-ions do not enter into the octahedral sites. Moreover, octahedral coordination has not been changed after irradiation also. After irradiation of both the pure ZnO and Co-doped ZnO samples some new peaks have been arisen at around 805 cm^{-1}, 1050 cm^{-1}, and 1260 cm^{-1}. These also may be assigned to C-O out of plane and CH_3 rocking mode, arising due to the surface modification due to chemical synthesis of the samples. However, since all the samples are synthesized by the same route by using the same batch of chemicals, it is unlikely to get C-O out of plane and CH_3 rocking mode only in the irradiated samples. Hence, these new peaks are definitely be related to the Co-O bond vibrations. More study is required to identify the nature of these modes. A broad absorption band at ~3460 cm^{-1} has been assigned to the stretching vibration mode of hydroxyl group. The band at ~1630 cm^{-1} has been marked to the first overtone of fundamental stretching mode of –OH[46,47]. These vibrations designate the presence of bound H_2O on the surface of the sample[48]. The peak around 2345 cm^{-1} is due to CO_2 molecules present in the citrate and in air. Another new peak around 2964 cm^{-1} has been observed in irradiated samples. All the vibrational bands have been assigned (ESI-4).

UV-Vis spectroscopy

UV–visible absorbance spectra of pristine and irradiated ZnO and Co-doped ZnO are shown in Fig. 6(a) and (b) respectively. The optical absorption measurements of the pristine and irradiated samples have been carried out by making thin layer of the samples on glass slide. The optical band gap has been evaluated using the relation:[49,50]

$$(\alpha h\nu)^2 = A(h\nu - E_g) \quad (5)$$

where A is a constant, h is the Planck's constant, ν is the frequency of light, and E_g is the band gap of the material. The direct transitions in this system have been confirmed from the linear fitting of the $(\alpha h\nu)^2$ *vs.* hν plot (inset figures). The optical band gap (E_g) has been estimated from the intercept of the linear portion of the plot to $(\alpha h\nu)^2 = 0$. The band gap measured for the pristine ZnO and Co-doped ZnO NPs close to the energy ~3.10 eV and ~3.15 eV respectively. The result shows that bandgap has increased due to Co-doping. This blue shift behavior or broadening in the band gap for Co2 sample with respect to the Co0 (ZnO) may be due to the 4*s* – *3d* and 2*p* –*3d* orbital electrons interactions in which decrease of Zn 3*d* electron density and the increase of Co 3*d* electron density below the valence band leads to higher binding energy of the valence band maximum giving rise to the larger bandgap.[20,51] This blue shift behaviour or broadening in the bandgap may also be due to the Burstein-Moss band filling effect.[52,53] After irradiation bandgap is decreased which may be due to the fact that ion irradiation has created some new localized energy states (defect states) above the valence band. It is a well known fact that the SHI beam induces point defects and extended defects on the target surface.[54] High fluence of ion-irradiation may create the huge number of defect states which act as trapping centers for charge carriers present in ZnO nanocrystals, leading to band bending near the surface.[55] It should be pointed out that the exponential edge (Urbach edge)[50] has been observed for all the samples (Fig. 7(a) and &(b)) which is generally related to the structural properties, impurity concentration, defect states, and preparation technique etc.[50,56] In the present case the grain boundaries[38,39] of the nono-grained particles (confirmed from AFM study) has played a significant role for the exponential edge. The exponential edge has been increased after the irradiation compared to its pristine counterpart (both for pure and doped samples) because of the fact that more defects have been created due to irradiation.

Photoluminescence (PL) spectroscopy

Photoluminescence (PL) spectra of pristine and irradiated pure ZnO nanocrystals under excitation of wavelength (λ_{ex}) of 320 nm are shown in Fig.7 (a) and those of Co-doped ZnO nanoparticles are shown in Fig.7 (b). Inset of (a) and (b) shows the de-convoluted PL intensities. Figure 7(a) & (b) show several peaks in PL spectra which are not sharp and found to be broad. This is may be because of the presence of several recombination sites, different impurities, grain boundaries and defects. The PL spectra (Fig. 7) show six peaks occurring around 380 nm, 406 nm, 432 nm, 461 nm, 485 nm and 525 nm. The first one is in the ultraviolet (UV) region, while other five correspond to violet, violet-blue, blue, blue-green and green respectively are in visible region. Typical PL spectra of pristine and irradiated ZnO sample exhibits UV emission at 380 nm. But since the defect-related emissions dominate, this near band-edge emission (NBE) at ~380 nm is poorly reveled. Moreover, NBE diminishes after irradiation because of the fact that more defect states have been introduced due to ion irradiation[57]. The UV emission band can be explained by a near band edge (NBE) transition originates from the recombination of carriers bound within excitons. For ZnO nanoparticles at room temperatures (T≥150 K), it is mostly due to recombination of the donor-bound excitons.[58] The energy gap between the bottom of the conduction band and the Zn vacancy (V_{Zn}) level is ~3.06 eV. So the violet emission around 406 nm (~3.06 eV) may be related to Zn vacancies.[59] The energy gap between interstitial Zn level (Zn_i) and the valence band is ~2.90 eV which is consistent with the energy of the violet-blue emission observed at 432 nm (~2.87 eV) in our experiment. The violet-blue and blue emission around 432 and 461 nm may also be attributed to the defect-related positively charged Zn vacancies.[60] It is observed from Figs. 7 (a) and (b) that the intensity of the emissions at 432 nm, 461 nm, 485 nm, and 525 nm (which are mainly related to the defect states) has been increased in irradiated samples compared to its pristine counterparts. In other words, ion irradiation has created the number of defect levels as has been reported earlier.[57]

Conclusion

In conclusion, nanocrystals of Co-doped ZnO have been synthesized using a sol-gel technique. XRD spectra indicate successful incorporation of cobalt ion in the ZnO lattice without any secondary phase. The pristine and Co-doped ZnO NPs were irradiated by using 200 MeV Ag^{15+} ion beam at fluence of 5×10^{12} ions/cm^2. Optical absorption (UV-vis) and PL properties also support dopant incorporation and effects of SHI irradiation on the nanoparticles. Due to

irradiation, surface roughness increases from 19 to 30 nm in case of pristine ZnO and 16 to 28 nm for 2% Co- doped ZnO nanoparticles. Increase in surface roughness may be due to the damage or defect created by the Ag^{15+} ions on the surface of the nanoparticles. AFM study shows prominent grain boundaries which played an important role in the optical properties (absorption and PL). Modifications in optical band gap were also observed as a result of the SHI irradiation which could be associated with the fact that ion irradiation may create some new localized energy states (defect states) above the valence band. This study demonstrates that SHI irradiation increases the photoluminescence intensity of the irradiated samples as compare to their pristine counterparts.

Acknowledgements

AKG is thankful to DAE-BRNS, India and CSIR, India for financial support (Grant No.: 2011/37P/11/BRNS/1038-1 and 03(1302)/13/EMR-II respectively), and to the Bio-Physics lab, Dept. of Physics for FTIR, UV-Vis and PL facilities.

References

1 J. K. Furdyna, J. Kossut, *Diluted Magnetic Semiconductors, (Semiconductors and Semimetals)*, Eds.; Academic Press: New York, Vol. 25,1988.

2 T. Dietl, H. Ohno, F. Matsukura, J. Cibert and D. Ferrand, *Science*, 1998, **281**, 951–956.

3 J. T. Chen, W. C. Lai, C. H. Chen, Y. Y. Yang, J. K. Sheu, K. W. Lin and L. W. Lai, *Opt. Express*, 2012, **20**, 19635–19642.

4 S. A. Wolf, , D. D. Awschalom, R. A. Buhrman, J. M. Daughton, S. von Molnar, M. L. Roukes, A. Y. Chtchelkanova and D. M. Treger, *Science*, 2001, **294**, 1488−1495.

5 Y. Ohno, D. K. Young, B. Beshoten, F. Matsukura, H. Ohno and D. D. Awschalom, *Nature*, 1999, **402**, 790−792.

6 S. K. Mandal, A. K. Das, T. K. Nath and D. Karmakar, *Appl. Phys. Lett*., 2006, **89**, 144105.

7 Shiv Kumar, K. Asokan, R. K. Singh, S. Chatterjee, D. Kanjilal and Anup K. Ghosh, *J. Appl. Phys.*, 2013,**114**, 164321.

8 Shiv Kumar, S. Chatterjee, K. K. Chattopadhyay and A. K. Ghosh, *J. Phys. Chem. C*, 2012, **116**, 16700−16708.

9 P. K. Sharma, R. K. Dutta, A. C. Pandey, S. Layek and H. C. Verma, *J. Magn. Magn. Mater.*, 2009, **321**, 2587–2591.

10 J. H. Kim, H. Kim, D. Kim, Y. E. Ihm and W. K. Choo, *J. Appl. Phys.,* 2002, **92**, 6066.

11 Z. H. Zhang, X. Wang, J. B. Xu, S. Muller, C. Ronning and Quan Li, *Nature Nanotechnology*, 2009, **4**, 523–527.

12 S. O. Kucheyev, J. S. Williams, C. Jagadish, J. Zou, C. Evans, A. J. Nelson and A. V. Hamza, *Phys. Rev. B: Condens. Matter Mater. Phys.*, 2003, **67**, 094115.

13 D. K. Shukla, R. Kumar, S. Mollah, R. J. Choudhary, P. Thakur, S. K. Sharma, N. B. Brookes and M. Knobel, *Phys. Rev. B: Condens. Matter Mater. Phys.,* 2010, **82**, 174432.

14 A. Kumar, M. K. Jaiswal, D. Kanjilal, R. K. Joshi and T. Mohanty, *Appl. Phys. Lett.* 2011, **99,** 013109.

15 J. F. Ziegler, J. P. Biersack and U. Littmark, *The Stopping and Range of Ions in Matter, Pergamon*, New York, 1985.

16 M. Nastasi, J. Mayer and J. Hirvonen, *Ion-Solid Interactions-Fundamentals and Applications,* Cambridge University Press, Cambridge, 1996.

17 D. C. Agarwal, A. Kumar, S. A. Khan, D. Kabiraj, F. Singh, A. Tripathi, J. C. Pivin, R. S. Chauhan and D. K. Avasthi, *Nucl. Instrum. Methods B*, 2006, **244**, 136–140.

18 J. B. Cui and U. J. Gibson, *Appl. Phys. Lett.*, 2005, **87**, 133108.

19 K. Ueda, H. Tabata and T. Kawai, *Appl. Phys. Lett.*, 2001, **79**, 988–990.

20 Shiv Kumar, S. Basu, B. Rana, A. Barman, S. Chatterjee, S. N. Jha, D. Bhattacharyya, N. K. Sahoo and Anup K. Ghosh, *J. Mater. Chem. C*, 2014, **2**, 481–495.

21 A. K. Zak, W. H. Abd. Majid, M. E. Abrishami and R. Yousefi, *Solid State Sci.*, 2011, **13** 251–256.

22 H. Morkoç and Ü. Özgür, *Zinc Oxide- Fundamentals, Materials and Device Technology,* WILEY-VCH Verlag GmbH, Germany, 2009.

23 Ü. Özgür, Ya. I. Alivov, C. Liu, A. Teke, M. A. Reshchikov, S. Doğan, V. Avrutin, S.-J. Cho and H. Morkoç, *J. Appl. Phys.,* 2005, **98**, 041301.

24 B. D. Cullity, *Elements of X-Ray Diffraction*, Addison-Wesley, MA, 1978.

25 A. L. Patterson, *Phys. Rev.,* 1939, **56**, 972–977.

26 E. Prince and J. K. Stalick, *Accuracy in Powder Diffraction II, NIST Special Publication,* Vol. **597,** 1992.

27 L. W. Yang, X. L. Wu, G. S. Huang, T. Qiu and Y. M. Yang, *J. Appl. Phys.*, 2005, **97**, 014308.

28 D. G. Mead and G. R. Wilkinson, *J. Raman Spectrosc.*,1977, **6**, 123–129.

29 J. M. Calleja and M. Cardona, *Phys. Rev. B: Condens. Matter Mater. Phys.*, 1977, **16**, 3753–3761.

30 X. Wang, J. Xu, X. Yu, K. Xue, J. Yu and X. Zhao, *Appl. Phys. Lett.*, 2007, **91**, 031908.

31 S. Singh and M. S. Ramachandra Rao, *Phys. Rev. B: Condens. Matter Mater. Phys.*, 2009, **80**, 045210.

32 J. Serrano, A. H. Romero, F. J. Manjo'n, R. Lauck, M. Cardona and A. Rubio, *Phys. Rev. B: Condens. Matter Mater. Phys.*, 2004, **69**, 094306.

33 R. Cusco, E. A. Llado, J. Ibanez, L. Artus, J. Jim´enez, B. G. Wang and M. J. Callahan, *Phys. Rev. B: Condens. Matter Mater. Phys.*, 2007, **75**, 165202.

34 X. B. Wang, C. Song, K. W. Geng, F. Zeng and F. Pan, *J. Phys. D: Appl. Phys.*, 2006, **39**, 4992–4996.

35 T. C. Damen, S. P. S. Porto and B. Tell, *Phys. Rev.*,1966, **142**, 570–574.

36 P. K. Giri, S. Bhattacharyya, D. K. Singh, R. Kesavamoorthy, B. K. Panigrahi and K. G. M. Nair, *J. Appl. Phys*., 2007,**102**, 093515.

37 X. W. Fu, Z. M. Liao, R. Liu, J. Xu and D. Yu, *ACS nano*, 2013, **7**, 8891–8898.

38 B. B. Straumal, S. G. Protasova, A. A. Mazilkin, T. Tietze, E. Goering, G. Schütz, P. B. Straumal and B. Baretzky, *Beilstein J. Nanotechnol.*, 2013, **4**, 361–369.

39 B. B. Straumal, A. A. Mazilkin, S. G. Protasova, P. B. Straumal, A. A. Myatiev, G. Schütz, E. Goering and B. Baretzky, *The Physics of Metals and Metallography*, 2012, **113**, 1244–1256.

40 M. Ulmeanu, A. Serghei, I. N. Mihailescu, P. Budau and M. Enachescu, *Applied Surface Science*, 2000, **165**, 109–115.

41 B. N. Dash, P. Mallick, P. Dash, R. Biswal, J. Prakash, A. Tripathi, D. Kanjilal and N. C. Mishra, *Bull. Mater. Sci.*, 2003, **36**, 813–818.

42 Jai Prakash, A. Tripathi, G. B. V. S. Lakshmi, V. Rigato, J. Tripathi and D. K. Avasthi, *Adv. Mat. Lett.*, 2013, **4(6)**, 408–412.

43 P. D. Cozzoli, M. L. Curri, A. Agostiano, G. Leo and M. Lomascolo, *Phys. Chem. B*, 2003, **107**, 4756–4762.

44 Y. Guo, X. Cao, X. Lan, C. Zhao, X. Xue and Y. Song, *J. Phys. Chem. C*, 2008, **112**, 8832–8838.

45 R. D. Waldron, *Phys. Rev.*, 1955, **99 (6)**, 1727–1735.

46 Y. M. Hao, S. Y. Lou, S. M. Zhou, R. J. Yuan, G. Y. Zhu and N. Li, *Nanoscale Res. Lett.* 2012, **7**,100.

47 J. B. Paul, R. A. Provencal, C. Chapo, K. Roth, R. Casaes and R. J. Saykally, *J. Phys. Chem. A*, 1999, **103**, 2972–2974.

48 G. H. Ning, X. Zhao and J. Li, *Opt. Mater.*, 2004, **27**, 1–5.

49 J. I. Pankove, *Optical Processes in Semiconductors*, Dover, New York, 1975.

50 J. Tauc, *Amorphous and Liquid Semiconductors,* New York: Plenum, 1974.

51 S. J. Gilliland, J. A. Sans, J. F. S´anchez-Royo, G. Almonacid, B. Garc´ıa-Domene, A. Segura, G. Tobias and E. Canadell, *Phys. Rev. B: Condens. Matter Mater. Phys.*, 2012, **86**, 155203.

52 E. Burstein, *Phys. Rev*., 1954, **93**, 632–633.

53 F. K. Shan and Y. S .Yu, *J. Eur. Ceram. Soc.*, 2004, **24**, 1869–1872.

54 P. K. Kulriya, B. R. Mehta, D. K. Avasthi, D. C. Agarwal, P. Thakur, N. B. Brookes, A. K. Chawla and R. Chandra, *Appl. Phys. Lett.*, 2010, **96**, 053103.

55 B. J. Morgan and G. W. Watson, *Phys. Rev. B: Condens. Matter Mater. Phys.*, 2009, **80**, 233102.

56 A. K. Ghosh, K. K. Som, S. Chatterjee and B. K. Chaudhuri, *Phys. Rev. B*: *Condens. Matter Mater. Phys.*, 1995, **51**, 4842–4848.

57 S. O. Kucheyev, J. S. Williams, C. Jagadish, J. Zou, Cheryl Evans, A. J. Nelson and A. V. Hamza, *Phys. Rev. B*: *Condens. Matter Mater. Phys.*, 2003, **67**, 094115.

58 V. A. Fonoberov, K. A. Alim, A. A. Balandin, F. Xiu and J. Liu, *Phys. Rev. B*: *Condens. Matter Mater. Phys.*, 2006, **73**, 165317.

59 B. Lin, Z. Fu and Y. Jia, *Appl. Phys. Lett.*, 2001, **79**, 943–945.

60 T. Kataoka, Y. Yamazaki, Y. Sakamoto, A. Fujimori, F.-H. Chang, H.-J. Lin, D. J. Huang, C. T. Chen, A. Tanaka, S. K. Mandal, T. K. Nath, D. Karmakar and I. Dasgupta, *Appl. Phys. Lett.*, 2010, **96**, 252502.

Figure Captions:

Fig. 1 Rietveld refinement of the X-ray diffraction patterns (a) pristine and irradiated pure ZnO and (b) pristine and irradiated Co-doped ZnO samples. The inset (i) and (ii) of figures (a) and (b) are the fitted curve of (101) plane for the corresponding pristine and irradiated samples.

Fig. 2 Room-temperature micro-Raman spectra of pristine and irradiated ZnO nanocrystals. Inset shows those of $Zn_{0.98}Co_{0.02}O$ nanocrystals.

Fig. 3 2D [(a) and (b)]- and 3D [(c) and (d)]- AFM images of pristine and irradiated ZnO nanocrystals.

Fig. 4 2D [(a) and (b)]- and 3D [(c) and (d)]- AFM images of pristine and irradiated Co-doped ZnO nanocrystals.

Fig. 5 FTIR spectra of pristine and irradiated pure and Co-doped ZnO nanocrystals.

Fig. 6 (a) Optical absorption spectra of pristine and irradiated ZnO nanoparticles. The inset shows the $(ah\nu)^2$ vs. $h\nu$ plot of those nanoparticles. (b) Optical absorption spectra of pristine and irradiated Co-doped ZnO nanoparticles. The inset shows $(ah\nu)^2$ vs. $h\nu$ plot of those nanoparticles.

Fig. 7 (a) PL spectra of pristine and irradiated pure ZnO nanocrystals excited at $\lambda_{ex} = 320$ nm and (b) those of Co-doped ZnO nanocrystals. Inset of (a) and (b) shows the de-convoluted PL intensity of the pure ZnO (pristine and irradiated) and Co-doped ZnO (pristine and irradiated), respectively.

Table 1. The crystallite size and average strain.

Table 2. Raman modes of pristine and irradiated samples.

Electronic information:

ESI-1: The lattice parameter *a* and *c*; interplanar spacing (d_{100}, d_{002}, and d_{101}); unit cell volume (V); *u* (length of the bond parallel to the *c* axis, in units of *c*); bond distance (*R*) and bond angles calculated from XRD data:

ESI-2: The liner fit $(d\beta Cos\theta/\lambda)^2$ vs. $(d^2\beta Cos\theta/\lambda^2)$ plot of the samples to estimate crystallite size and strain.

ESI-3: Intensity ratios of some of the Raman modes:

ESI-4:. Different Vibrational Modes of FTIR study:

Table 1. The crystallite size and average strain:

Sample	Crystallite Size (nm)		Strain
	Scherrer formula	Size-Strain Plot	Size-Strain Plot
Co0	39	42	1.6×10^{-3}
Co0 (5×10^{12})	42	45	2.0×10^{-3}
Co2	46	49	1.5×10^{-3}
Co2 (5×10^{12})	49	51	1.8×10^{-3}

Table 2. Raman modes of pristine and irradiated samples:

Vibration frequency (cm^{-1})				Assignments	Process
Co0	Co0 (5×10^{12})	Co2	Co2 (5×10^{12})		
329	330	329	331	E_{2H}-E_{2L}	Second order

379	-----	378	-----	A_1(TO)	First order
408	-----	-----	-----	E_1(TO)	First order
434	435	434	438	E_{2H}	First order
-----	-----	486	491	E_g	Dopant related
576	572	547	550	A_1(LO)	First order
585	-----	575	576	E_1(LO)	First order
658	694	682	707		Second order
1142	1138	1148	1138		Second order

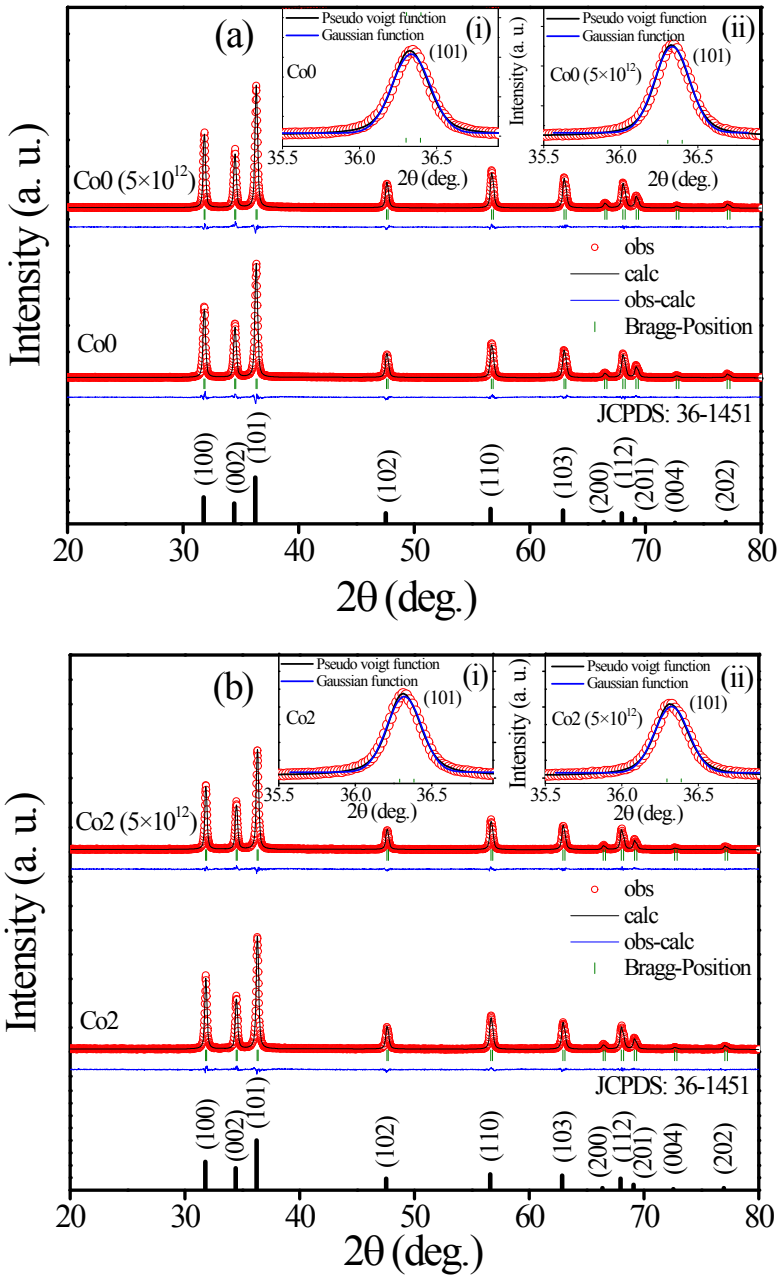

Fig. 1 Rietveld refinement of the X-ray diffraction patterns (a) pristine and irradiated pure ZnO and (b) pristine and irradiated Co-doped ZnO samples. The inset (i) and (ii) of figures (a) and (b) are the fitted curve of (101) plane for the corresponding pristine and irradiated samples.

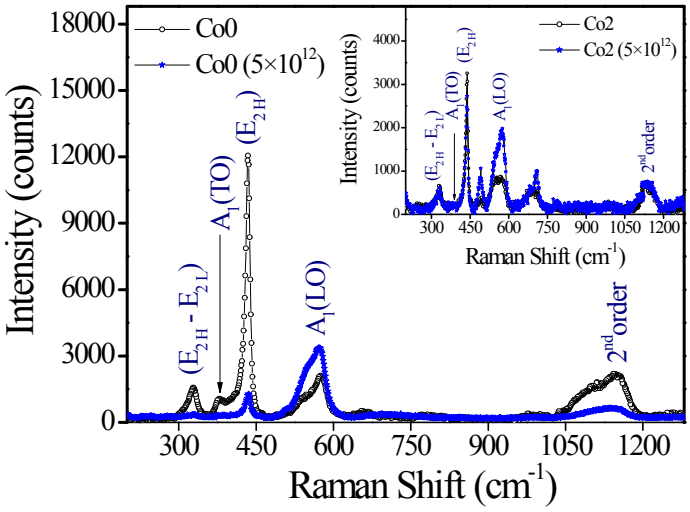

Fig. 2 Room-temperature micro-Raman spectra of pristine and irradiated ZnO nanocrystals. Inset shows those of $Zn_{0.98}Co_{0.02}O$ nanocrystals.

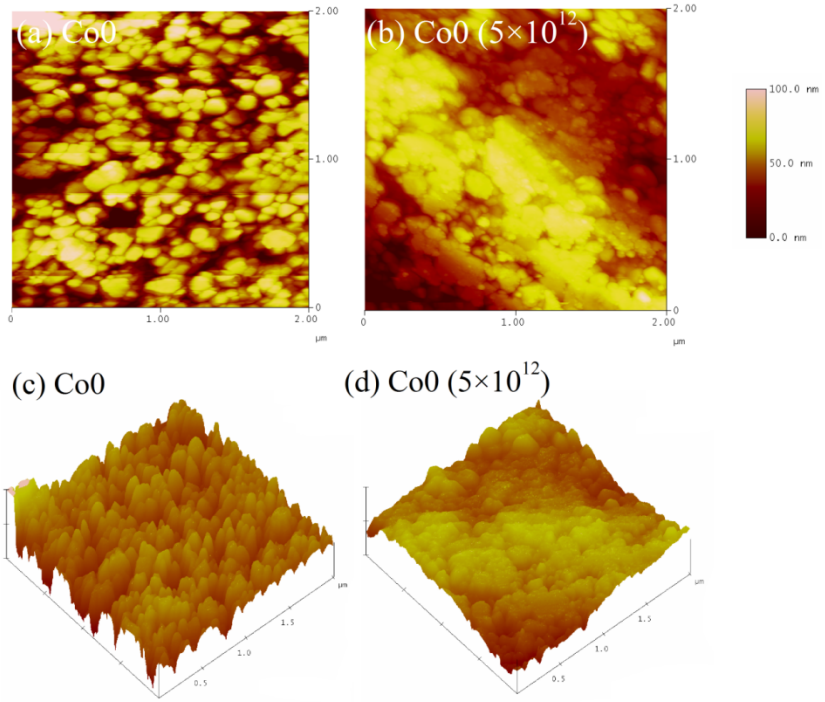

Fig. 3 2D [(a) and (b)]- and 3D [(c) and (d)]- AFM images of pristine and irradiated ZnO nanocrystals.

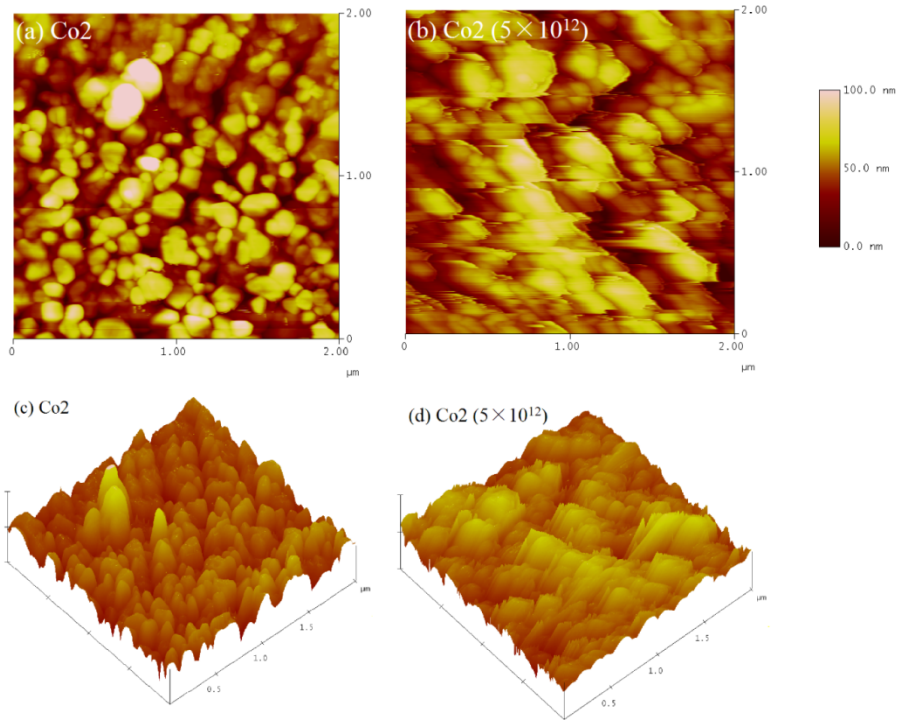

Fig. 4 2D [(a) and (b)]- and 3D [(c) and (d)]- AFM images of pristine and irradiated Co-doped ZnO nanocrystals.

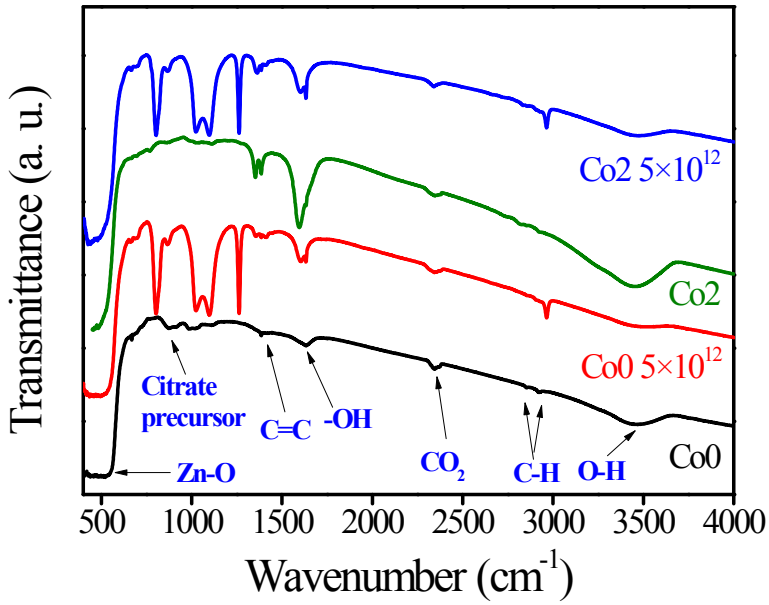

Fig. 5 FTIR spectra of pristine and irradiated pure and Co-doped ZnO nanocrystals.

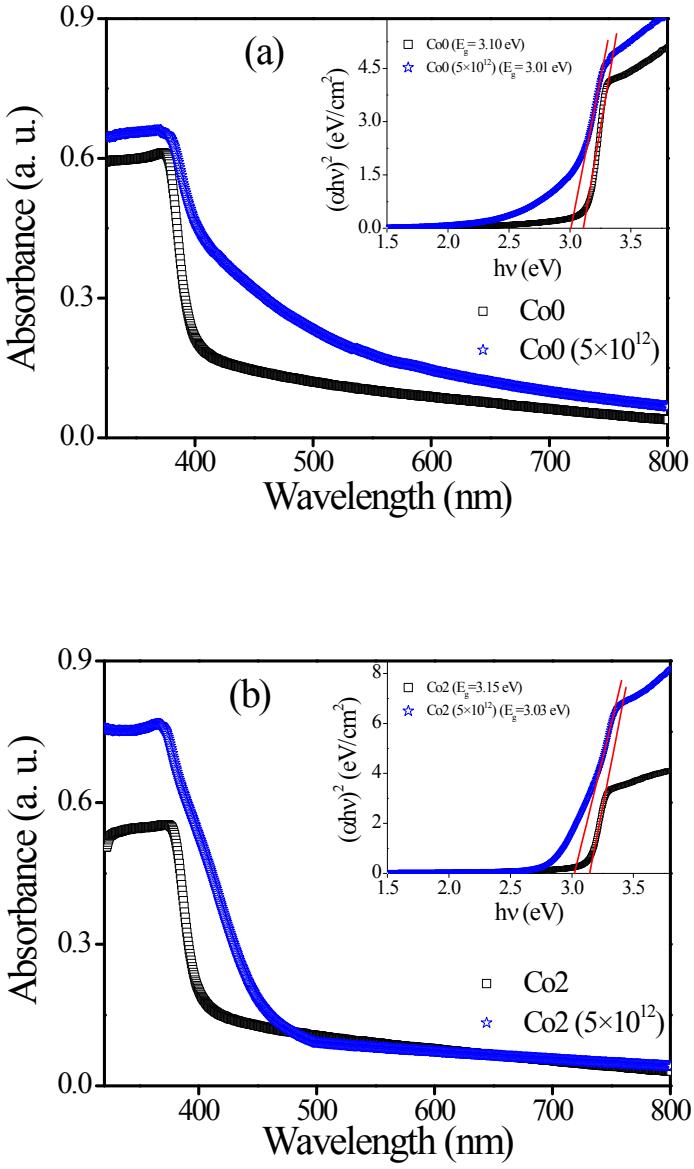

Fig. 6 (a) Optical absorption spectra of pristine and irradiated ZnO nanoparticles. The inset shows the $(ahν)^2$ vs. hν plot of those nanoparticles. (b) Optical absorption spectra of pristine and irradiated Co-doped ZnO nanoparticles. The inset shows $(ahν)^2$ vs. hν plot of those nanoparticles.

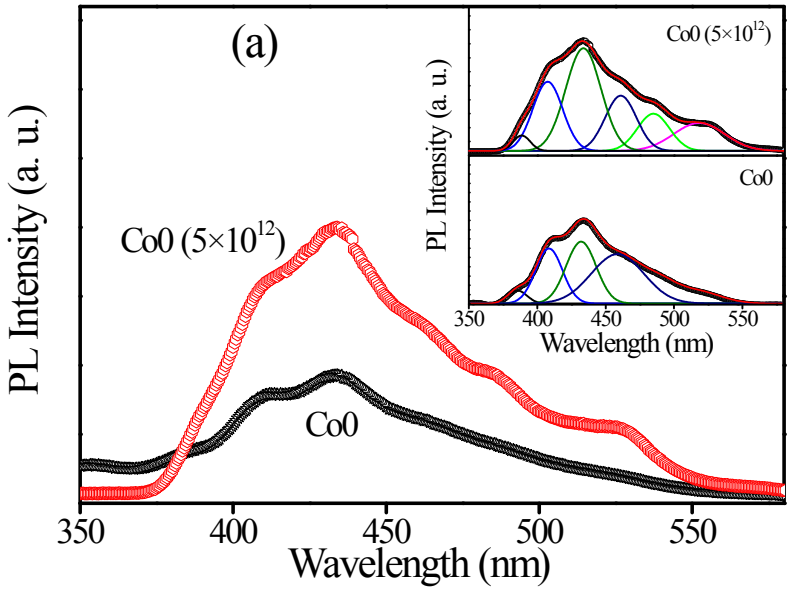
(a)
PL Intensity (a. u.)
Co0 (5×10^12)
Co0
350
400
450
500
550
Wavelength (nm)
PL Intensity (a. u.)
Co0 (5×10^12)
Co0
350
400
450
500
550
Wavelength (nm)

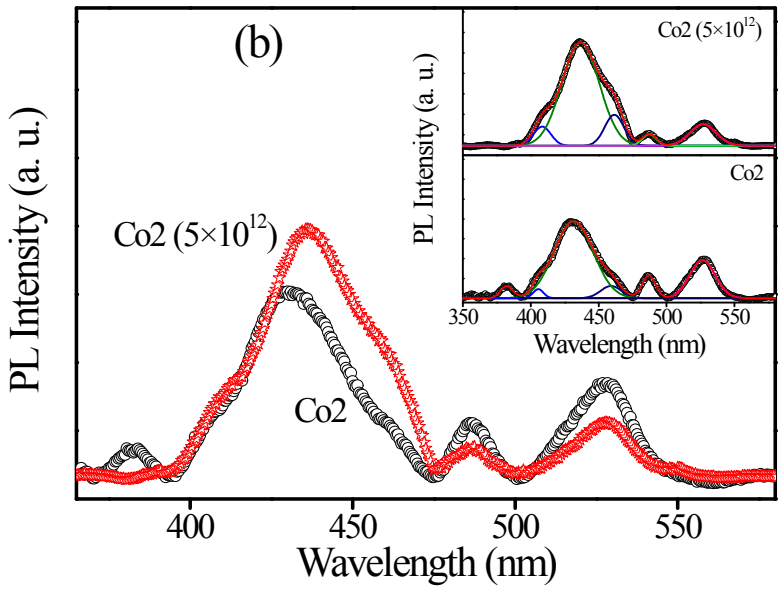
(b)
PL Intensity (a. u.)
Co2 (5×10^12)
Co2
400
450
500
550
Wavelength (nm)
PL Intensity (a. u.)
Co2 (5×10^12)
Co2
350
400
450
500
550
Wavelength (nm)

Fig. 7 (a) PL spectra of pristine and irradiated pure ZnO nanocrystals excited at λ_{ex} = 320 nm and (b) those of Co-doped ZnO nanocrystals. Inset of (a) and (b) shows the de-convoluted PL intensity of the pure ZnO (pristine and irradiated) and Co-doped ZnO (pristine and irradiated), respectively.